RESEARCH ARTICLE

ADVANCED MATERIALS TECHNOLOGIES
www.advmattechnol.de

Exceptional Performance of Room Temperature Sputtered Flexible Thermoelectric Thin Film Using High Target Utilisation Sputtering Technique

Xudong Tao, James Dutson, Chongyang Zeng, Ceyla Asker, Sally Luong, Abdallah Reza, Botao Hao, Zheng Zhang, Joshua Ellingford, Ruy Sebastian Bonilla, Oliver Fenwick, Emiliano Bilotti, Felix Hofmann, Mike Thwaites, and Hazel E. Assender*

The High Target Utilisation Sputtering technique (HiTUS) is of interest for industrial processes, including in roll-to-roll manufacturing. This study marks the first application of HiTUS to thermoelectric materials, exemplified by bismuth telluride. The HiTUS technique separates the sputtering power into the plasma power and the target power, with additional kinetic energy in the sputtering particles from the applied electrical field, thus enabling a much wider sputter parameter space to modify the film performance. This study investigates how plasma power, target power, and substrate bias in HiTUS intricately influence crystal orientation/size, elemental composition, surface morphology, and other film properties. These factors subsequently affect carrier density/mobility, and consequently the thermoelectric performance of the bismuth telluride film. These deposited films reach a power factor of 6.5×10^{-4} W m^{-1} K^{-2} with a figure of merit ≈0.14 at room temperature, the highest value for room-temperature sputtered un-doped bismuth telluride. Subsequent post-deposition annealing significantly enhances the crystallinity of the film (highly polycrystalline), further improving the power factor to 23.5 $\times 10^{-4}$ W m^{-1} K^{-2}, with a figure of merit ≈0.45 at room temperature. The excellent performance of the HiTUS fabricated thermoelectric film opens opportunities for the large-area manufacture of thin-film thermoelectric materials and devices.

1. Introduction

Flexible materials exhibit conformability and bendability and can be used to produce lightweight devices. Flexible thermoelectric (TE) materials are of increasing interest in the era of the Internet of Things (IoT), acting as a continuous/local power source for wearable sensors (e.g., temperature sensors,[1,2] pressure sensors,[3,4] humidity sensors[5,6]), biomedical sensors (e.g., cardiovascular monitors,[7,8] a glucose monitor[9]), and IoT-based devices (e.g., wearable sensor nodes[10–12]) or a direct sensor utilising the TE effect induced signals (e.g., a temperature sensor,[13] temperature-pressure sensors,[14–16] gas sensors,[17,18] infrared detection,[19] and an infrared display[20]).

Flexible TE materials have been extensively studied for decades in the laboratory, however, difficulty and cost of manufacture remain obstacles to a successful commercial implementation.[21] How to scale up the laboratory-fabricated

X. Tao, B. Hao, Z. Zhang, R. S. Bonilla, H. E. Assender
Department of Materials
University of Oxford
Parks Road, Oxford OX1 3PH, UK
E-mail: xt240@cam.ac.uk

J. Dutson, J. Ellingford, M. Thwaites
Plasma Quest Limited
Unit 1B Rose Estate, Osborn Way, Hook, Hampshire RG27 9UT, UK

C. Zeng, E. Bilotti
Department of Aeronautics
Imperial College London
Exhibition Road, London SW7 2AZ, UK

C. Asker, S. Luong, O. Fenwick
School of Engineering and Materials Science
Queen Mary University of London
Mile End Road, London E1 4NS, UK

A. Reza, F. Hofmann
Department of Engineering Science
University of Oxford
Parks Road, Oxford OX1 3PJ, UK

The ORCID identification number(s) for the author(s) of this article can be found under https://doi.org/10.1002/admt.202301958

© 2024 The Authors. Advanced Materials Technologies published by Wiley-VCH GmbH. This is an open access article under the terms of the Creative Commons Attribution License, which permits use, distribution and reproduction in any medium, provided the original work is properly cited.

DOI: 10.1002/admt.202301958

promising materials in a low-cost industrial manner, compatible with commercialisation, is crucial to fulfil an increasing demand in the era of IoT. Bulk thermoelectric materials fabricated through various techniques, such as sintering and hot pressing[22–25], consistently demonstrate excellent thermoelectric figures of merit. However, their limited mechanical flexibility hinders their use in flexible applications. Depositing thermoelectric materials as thin films on flexible substrates is a promising approach. Among various thin-film fabrication techniques,[26] the physical vapour deposition (PVD) processes, including sputtering and evaporation, show good compatibility with roll-to-roll (R2R) processing for flexible electronics. Sputtering is easier to control and has been often used to process functional materials including TE thin films. The recent development of flexible TE materials deposited by PVD in an R2R system marks significant progress for the manufacture in the thin-film form.[27–30] Thin-film TE materials have attracted widespread attention since the performance of TE materials can be modified using nanostructure engineering,[31] by decoupling the TE parameters shown in Equation (1). By further integrating the vacuum deposition with a flexographic printing technique,[32–34] patterning of flexible thin-film materials can be achieved at a μm resolution in the plane.

The thermoelectric figure of merit (ZT) is defined by:

$$ZT = \frac{S^2 \cdot T}{\rho \cdot \kappa} = PF \cdot \frac{T}{\kappa} \tag{1}$$

where ρ is the electrical resistivity, S is the Seebeck coefficient, κ is the thermal conductivity, PF is the power factor, T is the absolute temperature.

Previous studies successfully optimised the TE performance of sputtered bismuth telluride (Bi-Te) grown on flexible polymer sheets using an industry-scale R2R facility.[27–29] However, the TE performance (PF) remained low (14×10^{-4} W m^{-1} K^{-2}) as compared to a single crystal bulk Bi-Te (58×10^{-4} W m^{-1} K^{-2}).[35] By contrast, the fabrication of highly crystalline systems or single crystals needs an extremely hot substrate during deposition and high-temperature post-deposition annealing – neither of which are compatible with processing in R2R.

A novel sputtering technique, High Target Utilisation Sputtering (HiTUS), is particularly interesting in fabricating highly crystalline thin films. HiTUS sputtering can offer many advantages over traditional magnetron sputtering, especially for the possibility of minimising the waste of target materials, thus decreasing the manufacturing cost. HiTUS sputtering remotely generates plasma which is then guided toward the target source with a target bias for sputtering. This enables the full surface erosion of the target source materials, eliminating the racetrack issue commonly seen in conventional magnetron sputtering. Additionally, the density and energy of the plasma are independent of each other, controlled by the power on the plasma generator and the target source, respectively. This enables a much wider sputtering parameter space for optimisation of the film performance.

This is the first study employing the HiTUS technique to fabricate TE materials. The effect of HiTUS parameters (the plasma power, the target power, and the substrate bias) and post-deposition annealing conditions on the TE properties have been explored. In particular, Bi-Te is investigated, since it is one of the most important TE materials, presenting one of the highest values of TE efficiency near room temperature.[36]

2. Results and Discussion

2.1. Film Thickness and Sputter Rate

The Be-Te film thickness was controlled to be 520 (±47) nm, which can be confirmed by Dektak and scanning electron microscope (SEM) cross-sectional views (see Figures S1,S2, Supporting Information). Figure S2 (Supporting Information) illustrates the linear relationship between the sputtering rate and the plasma/target powers within the range of parameters applied. The plasma power and the target power have a positive effect on the sputtering rate because a higher-energy and denser plasma was generated leading to more sputtered species reaching/depositing onto the substrate. Regarding the effect of the substrate bias on the deposition rate, the rate remains constant until a significant substrate bias is applied (e.g., 120 W), ascribed to the effect of re-sputtering of the deposited film as the high bias attracts the ionised plasma flux toward the substrate holder, as observed in.[37]

2.2. Phase Identification

The phase of the Bi-Te thin film is identified by x-ray diffraction (XRD) and high-resolution transmission electron microscope (HRTEM). In **Figure 1a**, the main XRD peaks at (0 1 5), (1 0 10), (1 1 15) and (0 1 20), are consistent with the phase of Bi_2Te_3 (Inorganic Crystal Structure Database, ICSD, #193 330). As the plasma power is increased, small peaks (Bi_2Te_3 phase) at (0 1 11), (0 0 15), and (1 0 16) appear. On increasing the substrate bias, the peak at (1 0 10) diminishes while the peak at (0 0 15) grows. A sharp peak at (1 0 13) appears under a substrate bias of 125 W. For a substrate bias ≥100 W, two new peaks at 18.4° and 20.8° appear which cannot be identified for the phase of Bi_2Te_3. The film after annealing presents a polycrystalline structure, with more Bi_2Te_3 peaks appearing, e.g., (0 0 6), (0 1 8), (1 1 6), (0 2 10), (0 2 16), and (2 1 13). Two peaks at 18.6° and 55.1° cannot be attributed to the Bi_2Te_3 phase for the post-annealed samples under 400 and 450 °C (see Figure S3a, Supporting Information).

Although some d-spacings (see Table S1, Supporting Information) cannot be obtained from XRD analysis of the as-deposited 500-nm thick film (because of insufficient signal from the XRD characterisation), HRTEM images (Figure 1) and fast Fourier transform images (Figure S3, Supporting Information) confirm a polycrystalline structure of an as-fabricated ≈50-nm thick film (without subsequent anneal). In Table S1 (Supporting Information), all d-spacings (except 3.95 Å) from HRTEM can be confirmed by XRD of the annealed 500-nm thick film. The crystallite size (Figure 1e) slightly increases as the target power and the plasma power increase but is constant (within error) with substrate bias until an ultra-high bias, e.g., 125 W (associated with re-sputtering, see Figure S2d, Supporting Information) is applied. At the same high substrate bias, there is an observed change in the peaks in XRD, notably with a prominent (1 0 13) peak replacing the previously observed (1 0 10) peak. The crystallite size

© 2024 The Authors. Advanced Materials Technologies published by Wiley-VCH GmbH

2365709x, 0, Downloaded from https://onlinelibrary.wiley.com/doi/10.1002/admt.202301958 by Test, Wiley Online Library on [08/02/2024]. See the Terms and Conditions (https://onlinelibrary.wiley.com/terms-and-conditions) on Wiley Online Library for rules of use; OA articles are governed by the applicable Creative Commons License

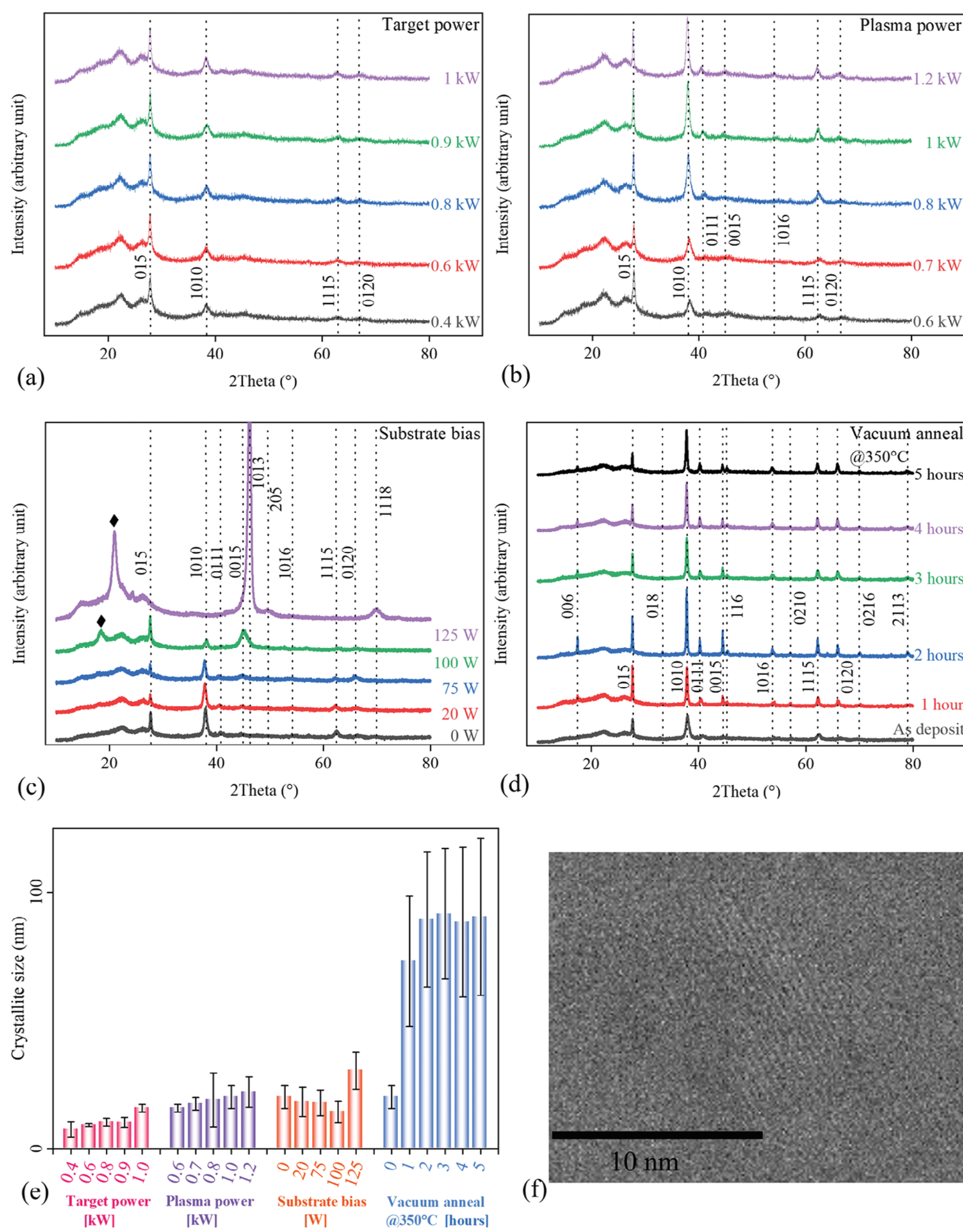

Figure 1. XRD profiles of films sputtered with various target powers a), plasma powers b), substrate bias c), and 350 °C anneals d); e) Crystallite size of various films; f) HRTEM image of a ≈50-nm thick Bi-Te film (without subsequent anneal). In the XRD figures, the vertical reference lines correspond to the standard Bi_2Te_3 reference (ICSD #193 330). The rhombus symbol in (c) is used to indicate a peak that cannot be identified by the standard reference.

increases with the annealing temperature (see Figure S4, Supporting Information), and it broadly remains constant at a fixed annealing temperature (350°C) with varying annealing time from 1 to 5 h (Figure 1e).

For PVD at room temperature, the film crystallinity has been reported to be strongly dependent on the kinetic energy of sputtered atoms arriving on the substrate, i.e., the ability to self-organise during nucleation and film formation.[38] The kinetic energy of sputtered atoms can be affected by the substrate bias (by attracting/splitting the plasma flux from the plasma generator, toward the substrate holder), and by the energy conversion (i.e., the bombardment on the surface of target materials) from the energetic plasma (controlled by the plasma power and the target power in HiTUS). With the HiTUS system, these can be independently varied, providing a useful study of the deposition of ordered materials at room temperature, and the plasma power, the target power and the substrate bias can be optimised in the HiTUS system for improving crystallinity.

In HiTUS, as the plasma power increases, the plasma current increases (I_p↑) but the plasma voltage decreases (V_p↓); as the target power increases (for constant plasma power), the target voltage increases (V_t↑) but the target current is fixed ($I_t =$), because it is coupled with the plasma current. I_p is dominated by the plasma density while the kinetic energy of the plasma depends on V_p and

© 2024 The Authors. Advanced Materials Technologies published by Wiley-VCH GmbH

2365709x, 0, Downloaded from https://onlinelibrary.wiley.com/doi/10.1002/admt.202301958 by Test, Wiley Online Library on [08/02/2024]. See the Terms and Conditions (https://onlinelibrary.wiley.com/terms-and-conditions) on Wiley Online Library for rules of use; OA articles are governed by the applicable Creative Commons License

V_t. Hence, one might expect that the crystallinity might depend on V_p and V_t.

In Figure 1a, however, as the target power increases, there is no obvious change in crystallinity indicated by the intensities of the main XRD peaks (0 1 5) and (1 0 10), and only a slight increase in the crystallite size (see Figure 1e) calculated from the peak widths. At greater plasma power, despite the decrease in V_p, there is an observed increase in the peak (1 0 10) (see Figure 1b), rather than the expected decrease in crystallinity. In the HiTUS system, a magnetic field is applied by an electromagnet to lead/bend the plasma. It has been reported that 50% of the magnetic energy was converted to the particle energy in the plasma,[39] i.e., the kinetic energy of the plasma, which could be dominant instead of the kinetic energy originating from V_t or V_p. This is consistent with the observed negligible change in crystallinity (Figure 1a) as $V_t\uparrow$. In terms of an increase in crystallinity with $V_p\downarrow$ (Figure 1b), it could be explained by a denser plasma induced by $I_p\uparrow$, causing an atomic peening mechanism[40] or an annealing effect on the film by the near-substrate plasma.[41,42] Similarly, the substrate bias also alters the "near-substrate" plasma density, modifying (or for very high bias, re-sputtering) the surface of the as-grown film, or affecting the atomic direction and the kinetic energy of sputtered species,[37] perhaps explaining the change in the orientational population of the crystals from (1 0 10) to (1 0 13) in Figure 1c.

Energy dispersive x-ray spectroscopy (EDX) confirms the Bi-Te composition. Figure S4e,f (Supporting Information) illustrates a uniform distribution of the Bi and Te elements in the film. We observed a constant ratio of Te: Bi atomic% regardless of sputter conditions, becoming more Bi-rich only in the cases of the greatest substrate biases (when re-sputtering occurs) or when a high-temperature/long-time post-annealing treatment is applied (see **Figure 2u**; Figure S4g, Supporting Information). This phenomenon is consistent with the observation in XRD of non-Bi_2Te_3 peaks (Figure 1c; Figure S3a, Supporting Information), which we attribute to a re-sputtering or vaporisation of Te under a significant substrate bias or an extreme annealing treatment.

2.3. Surface Morphology

Figure 2 and **Figure 3** present the surface morphologies of Bi-Te films. As the target power increases, there are no obvious changes in morphology as observed by SEM and atomic force microscopy (AFM), while the results of root mean square roughness (RMSR) and grain size (Figure 3u) indicate a slight grain growth and surface flattening. The increase in the plasma power causes a finer grain size and a much smoother surface, attributable to a much denser plasma induced by the plasma power (similarly to the observation while increasing the plasma density by gas pressure in direct-current magnetron sputtering[28]). It is noted that the grain size and RMSR start to increase at a high plasma power of 1.2 kW. With increasing substrate bias, the atomic-peening-induced modification increases the grain size, but the surface roughness also increases. As the substrate bias increases from 100 to 125 W, a much smaller grain size is observed, presumably due to significant re-sputtering. In terms of the post-annealed samples, an increase in grain size is observed in both AFM and SEM images after annealing with increasing annealing temperatures in the range of 350°C to 450°C (see Figure S4, Supporting Information). The sample annealed at 450 °C exhibits large grains with trigeminal grain boundaries with 120° angles ascribed to a coalescence/rearrangement during 450 °C ultra-high temperature annealing. Slight increases in grain size and RMSR are observed as the annealing time increases from 1 to 5 h at a temperature of 350 °C (Figure 3u). The grain size observed from AFM and SEM is much larger than the crystallite size calculated from XRD (Figure 1e), indicating that a grain does not represent a single crystal.

Thus, the plasma and target powers during the HiTUS sputtering make a significant difference to the deposition rate, as would be expected, but also affect, differently, the surface roughness and formation of crystals. The substrate bias has a significant effect on the morphology and, at high bias, the composition of the films, indicating the critical role of plasma interaction with the depositing film on subsequent properties. This plasma interaction can be better controlled with the HiTUS system compared with conventional sputtering, as the HiTUS can independently control the plasma generation (plasma power) and target interaction (target power) due to the remote generation of the plasma from the target and the sample. We have observed the impact of this on film properties. As reported previously[29] in room-temperature sputtered Bi-Te films, post-deposition annealing of the substrate can affect the morphology, crystallinity and composition of the substrate from the "base-line" as-deposited films. The effects of these observed differences in process parameters on TE properties are explored in the next section.

2.4. Thermoelectric Characterisation of HiTUS Sputtered Bi-Te

2.4.1. Power Factor

The relationship in equation (1) suggests that a high S and low ρ are required for high TE performance, however S and ρ are coupled as increasing S is usually accompanied by increasing ρ.[43] Modification to the semiconductor nanostructure enables an increasing PF by going some way to change these TE parameters, and examination of the different HiTUS sputtering parameters can inform such changes. In the case of the HiTUS sputtered Bi-Te, we observe (**Figure 4**): 1) a negligible change in S (considering systematic error) with a decrease in ρ as increasing target power; 2) an increase in S and a decrease in ρ with increased plasma power; and 3) an increase in S with a constant ρ after 2-h annealing at 350 °C. Hence, a tweak of the process parameters allows a change in the relationships between S and ρ, which can give rise to an improvement in PF from 3.2 to 6.5×10^{-4} W m^{-1} K^{-2} after optimisations on the plasma power (1 kW) and the target power (1 kW) in HiTUS. To the authors' knowledge, this is the highest value of PF for room-temperature sputtered Bi-Te (see Figure S6, Supporting Information). The main measured difference between the HiTUS sputtered Bi-Te and a direct-current magnetron sputtered Bi-Te is the surface roughness and the crystallinity (see Figure S7, Supporting Information).

After post-deposition annealing, the highest PF is achieved for the Bi-Te film annealed at 350 °C for 2 h (23.5×10^{-4} W m^{-1} K^{-2}), which ranks at the top for sputtered pure/un-doped Bi-Te thin film, although it remains lower than the bulk crystalline Bi-Te

© 2024 The Authors. Advanced Materials Technologies published by Wiley-VCH GmbH

2365709x, 0, Downloaded from https://onlinelibrary.wiley.com/doi/10.1002/admt.202301958 by Test, Wiley Online Library on [08/02/2024]. See the Terms and Conditions (https://onlinelibrary.wiley.com/terms-and-conditions) on Wiley Online Library for rules of use; OA articles are governed by the applicable Creative Commons License

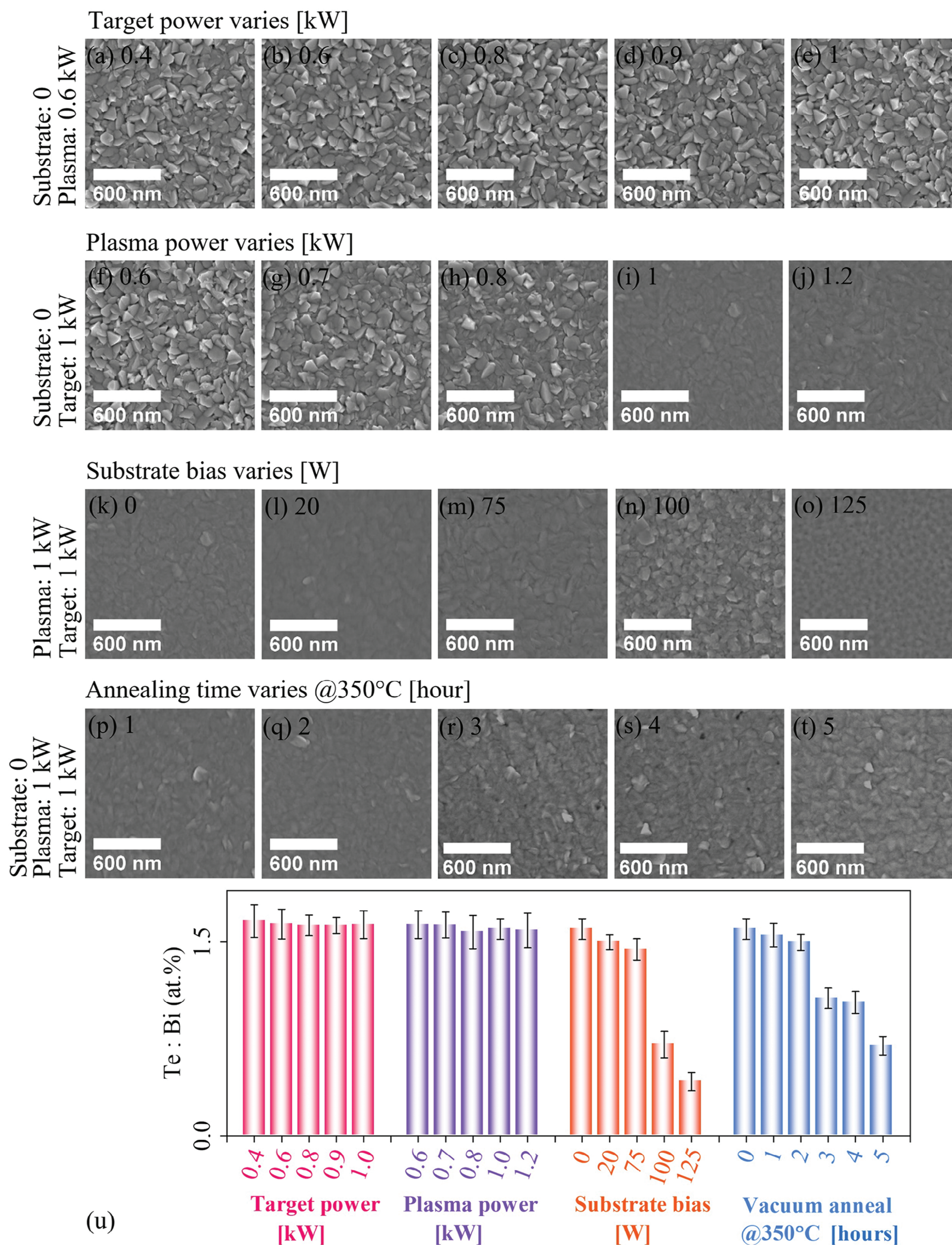

Figure 2. SEM images with variations in target powers a–e), plasma powers f–j), substrate bias k–o), and annealing time p–t); u) the elemental composition of respective films. It is noted that no post-deposition annealing was applied to the specimen a–o), and the accompanying text on the left indicates the fixed parameters in HiTUS.

© 2024 The Authors. Advanced Materials Technologies published by Wiley-VCH GmbH

2365709x, 0, Downloaded from https://onlinelibrary.wiley.com/doi/10.1002/admt.202301958 by Test, Wiley Online Library on [08/02/2024]. See the Terms and Conditions (https://onlinelibrary.wiley.com/terms-and-conditions) on Wiley Online Library for rules of use; OA articles are governed by the applicable Creative Commons License

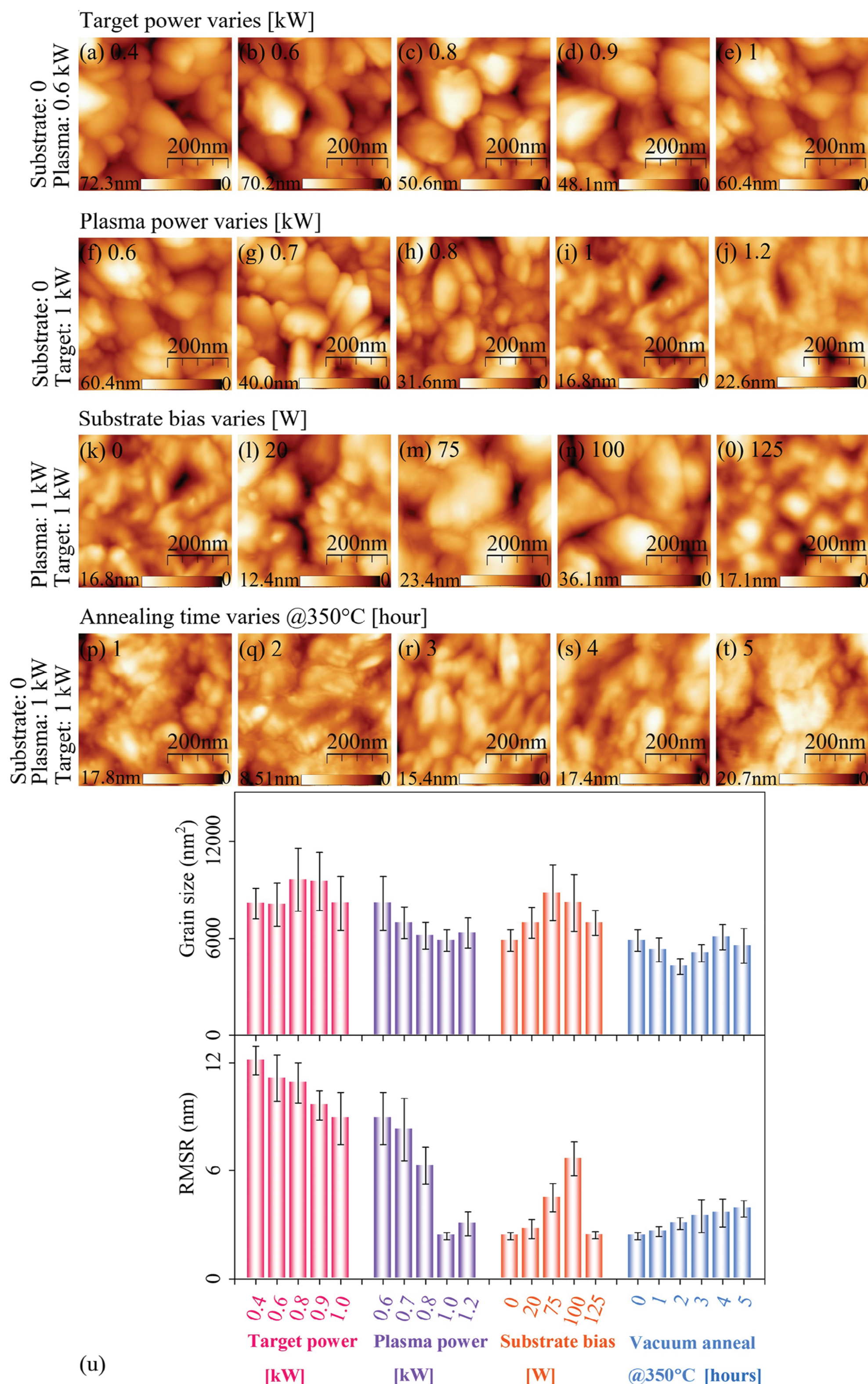

Figure 3. AFM images with variations in target powers a–e), plasma powers f–j), substrate bias k–o), and annealing time p–t); u) the grain size and surface roughness of respective films (the grain size is analysed from MIPAR software, see Figure S5, Supporting Information). It is noted that no post-deposition annealing was applied to the specimen a–o), and the accompanying text on the left indicates the fixed parameters in HiTUS.

© 2024 The Authors. Advanced Materials Technologies published by Wiley-VCH GmbH

2365709x, 0, Downloaded from https://onlinelibrary.wiley.com/doi/10.1002/admt.202301958 by Test, Wiley Online Library on [08/02/2024]. See the Terms and Conditions (https://onlinelibrary.wiley.com/terms-and-conditions) on Wiley Online Library for rules of use; OA articles are governed by the applicable Creative Commons License

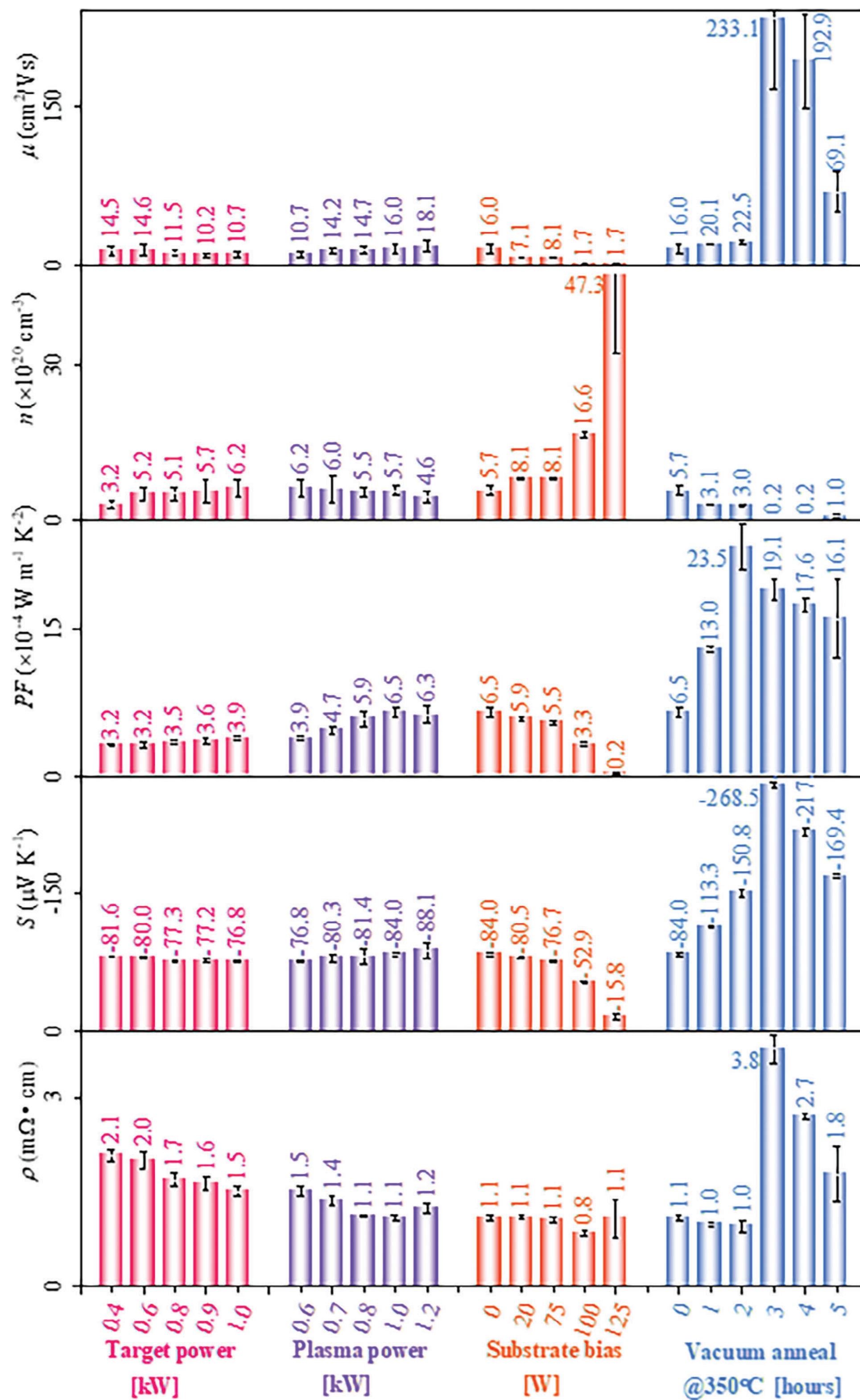

Figure 4. Electrical resistivity, Seebeck coefficient, power factor, carrier concentration and carrier mobility of various films, measured at room temperature. The negative value of S reveals that the majority of charge carriers are electrons thus the HiTUS sputtered Bi-Te is n-type. The samples were deposited under various conditions, grouped as follows: target power group (0.6 kW plasma power, no substrate bias/annealing), plasma power group (1 kW target power, no substrate bias/annealing), substrate bias group (1 kW plasma power/target power, and no annealing), and vacuum anneal group (1 kW target power/plasma power, and no substrate bias).

 © 2024 The Authors. Advanced Materials Technologies published by Wiley-VCH GmbH

2365709x, 0, Downloaded from https://onlinelibrary.wiley.com/doi/10.1002/admt.202301958 by Test, Wiley Online Library on [08/02/2024]. See the Terms and Conditions (https://onlinelibrary.wiley.com/terms-and-conditions) on Wiley Online Library for rules of use; OA articles are governed by the applicable Creative Commons License

(see Figure S6, Supporting Information). Nevertheless, the thin-film configuration has many advantages, especially in the application of flexible electronics.

S and ρ strongly depend on n and μ. As expected, the measured S and ρ fit well with the relation: $S \propto \mu^{0.2}$,[44] $\rho \propto 1/(\mu \cdot n)$,[45] $S \propto 1/(n^{2/3})$[46] (see **Figure 5**a–c). As reported in,[29] the behaviours of n and μ as well as their product, ρ, are correlated with several factors, e.g., the grain size, crystallite size, elemental composition, bandgap (E_g) and surface roughness (Figure 5):

(1) Figure 5d: As the crystallite size decreases, ρ increases because of a stronger carrier scattering effect with an increasing number of crystallites.

(2) Figure 5e: As the grain size decreases, μ increases which could be attributed to the carrier energy filtering effect (see Figure S8, Supporting Information) since more grain boundaries increase the probability of a higher energy barrier at the boundary.

(3) Figure 5f: A rougher surface – particularly in thin films exhibiting a strong surface effect – causes a higher ρ due to a greater scattering effect,[47] in addition to the effect of changes to the contact resistance between the probe and the film surface during the measurement.

(4) Figure 5g: As the Te:Bi atomic% increases, ρ increases, because the Te-rich phase or amorphous materials could have a higher electrical resistivity than the Bi-Te phase.

(5) Figure 5h,i: With increasing Te content in the film, the (in-)direct E_g increases, which could be attributed to a greater E_g of the Te-rich materials leading to an E_g transition.

(6) Figure 5j,k: n and ρ should be correlated with (in-)direct E_g (where $E_g\downarrow$ then $\rho\downarrow$) because a smaller E_g benefits exciting the valence-band electrons to the conduction band.[48] The relationship between ρ and E_g is clear, but the correlation between n and E_g (see Figure S9, Supporting Information) is not apparent, possibly due to the influence of other factors such as the film composition.

(7) Figure 5l: The observed XRD intensity of (1 0 10) seems to correlate well with the PF of the film. We might expect that if the greater intensity of the XRD peak reflected a higher crystallinity, this would be the case. However, where there is a significant difference in orientation or phase (with high annealing temperatures or highest biases, see Figure 1c; Figure S3a, Supporting Information) this correlation could be lost (see Figure 4; Figure S4, Supporting Information).

These observed trends are generally in line with expectations, but it is crucial to note that the changes in film properties are not solely governed by a single factor. Certain relationships in n and μ show no correlations (see Figure S9, Supporting Information). Therefore, the observed variations in thermoelectric TE performance result from a complex interplay of multiple factors, including grain size, crystallite size, crystal orientation, elemental composition, surface roughness, bandgap, etc. These factors enable alterations between the thermoelectric parameters (S and ρ), thus contributing to an increase in the thermoelectric power factor.

The HiTUS technique enables the separation of the conventional sputtering power into the plasma power and the target power. As the first study of HiTUS-fabricated thermoelectric materials, variation of the HiTUS parameters can allow different trends in the thermoelectric parameters and thus optimisations can lead to enhanced performance, by the modifications of carrier density and mobility which originate from the change in morphology (grain size/roughness), elemental composition, bandgap, and crystallinity (the crystal orientation/crystallite size). From this optimised base, post-annealing further enhances film crystallinity, increasing the film performance PF by more than three-fold.

Table 1. Results of thermal conductivity and figure of merit.

	Calculated		Transient grating spectroscopy	
	κ / W m^{-1} K^{-1}	ZT @300K	κ / W m^{-1} K^{-1}	ZT @300K
As-deposited	1.37 (±0.08)	0.14 (±0.01)	1.50 (±0.01)	0.13 (±0.01)
350 °C-2 h annealed	1.48 (±0.13)	0.47 (±0.06)	1.70 (±0.01)	0.40 (±0.05)

2.4.2. Thermal Conductivity and Figure of Merit

The electronic thermal conductivity (κ_e) calculated (see Appendix for details) from measurements of ρ of as-deposited, 350 °C-1 h annealed and 350 °C-2 h annealed specimens are 0.676 (±0.062), 0.741 (±0.030) and 0.756 (±0.129) W m^{-1} K^{-1} respectively; the calculated lattice thermal conductivity (κ_L) (see Figure S10, Supporting Information) are 0.694 (±0.015), 0.725 (±0.006), 0.728 (±0.005) W m^{-1} K^{-1}@300K, respectively. Hence, the total κ of the as-deposited, 350 °C-1 h annealed and 350 °C-2 h annealed specimens are expected to be 1.370 (±0.077), 1.466 (±0.036), 1.484 (±0.134) W m^{-1} K^{-1} @300K respectively, corresponding to a ZT of 0.14 (±0.01), 0.27 (±0.01), 0.47 (±0.06) @300K (**Table 1**). All the experimental results for calculation of κ_e and κ_L were acquired from the "polyimide sample", i.e., the Bi-Te film grown on a flexible polyimide sheet. Experimental values of crystallite size and film thickness for the "polyimide sample" were used with material properties from the literature in the Debeye-Callaway model for the calculation of κ_L (see Appendix for details). The limitation of this calculation is acknowledged, recognizing that material properties obtained from the literature may not precisely represent the characteristics of HiTUS-sputtered bismuth telluride under various fabrication conditions. Hence, we pursued two experimental methods to directly measure κ. 1) Pseudo steady-state 3-ω method[49,50]: the film deposited on the measurement chip may exhibit different properties than that deposited on the polyimide sheet, resulting in a significant difference in κ (Table S3, Supporting Information). 2) Transient grating spectroscopy: the thermal diffusivity of the "polyimide sample" (as deposited and 350 °C-2 h) was measured using the laser-induced transient grating spectroscopy method[51,52] giving values of 1.2 (±0.06) and 1.4 (±0.07) × 10^{-6} m^2 s^{-1}, respectively (see Figure S11, Supporting Information). Thus the total κ is calculated to be 1.5 (±0.1) and 1.7 (±0.1) W m^{-1} K^{-1}, corresponding to a ZT of 0.13 (±0.01) and 0.40 (±0.05) @300K (showing good agreement with the calculated values of ZT). For the calculation of κ using this means, it is noted that the thermal diffusivity is measured directly for the "polyimide sample" while literature values were used for the mass density and specific heat capacity.[53]

The experimental result of the laser-induced transient grating spectroscopy is closer to the calculated result and is more

© 2024 The Authors. Advanced Materials Technologies published by Wiley-VCH GmbH

2365709x, 0, Downloaded from https://onlinelibrary.wiley.com/doi/10.1002/admt.202301958 by Test, Wiley Online Library on [08/02/2024]. See the Terms and Conditions (https://onlinelibrary.wiley.com/terms-and-conditions) on Wiley Online Library for rules of use; OA articles are governed by the applicable Creative Commons License

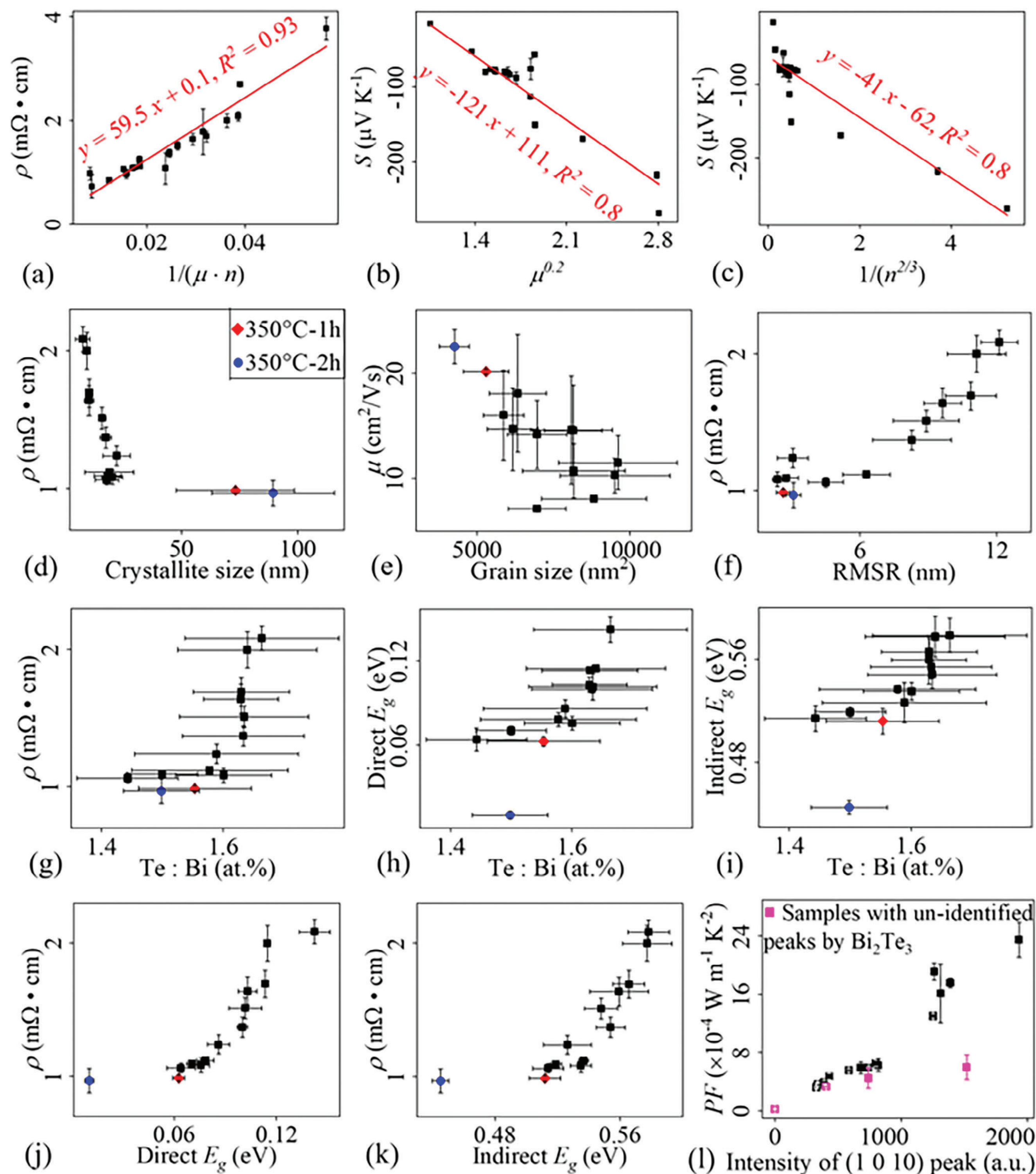

Figure 5. Relations of a) ρ versus $1/(\mu{\cdot}n)$; b) S versus $\mu^{0.2}$; c) S versus $1/(n^{2/3})$; d) Electrical resistivity versus crystallite size; e) Carrier mobility versus grain size; f) Electrical resistivity versus surface roughness; g–i) Elemental composition versus electrical resistivity and bandgap; j,k) Electrical resistivity versus bandgap; l) A plot of the intensity of the XRD peak (1 0 10) versus *PF*. (Note: the samples with the unidentified peak of Bi_2Te_3 are not considered in this figure.).

© 2024 The Authors. Advanced Materials Technologies published by Wiley-VCH GmbH

2365709x, 0, Downloaded from https://onlinelibrary.wiley.com/doi/10.1002/admt.202301958 by Test, Wiley Online Library on [08/02/2024]. See the Terms and Conditions (https://onlinelibrary.wiley.com/terms-and-conditions) on Wiley Online Library for rules of use; OA articles are governed by the applicable Creative Commons License

reliable because it is obtained from the sample on the polyimide substrate. The ZT of the 350 °C-2 h sample, 0.4 (the experimental) and 0.47 (the calculated) @300K, is much higher than that reported for the sputtered Bi-Te film grown under a hot condition, i.e., hot-substrate sputtering with post-anneal (0.2 @300K,[54] 2021), and is even comparable to the synthesised materials: 0.1–0.45 @300K, for un-doped Bi-Te.[55–59] In addition to excellent thermoelectric performance, it is worth noting that our HiTUS sputtering technique is compatible with R2R manufacturing, and, most importantly, it significantly reduces manufacturing costs by minimizing the waste of target materials, in contrast to conventional sputtering techniques.

2.4.3. Thermoelectric Performance of TEGs

The TE performance of the TEG device is given in **Figure 6**. The TEG performance reflects the materials performance as analysed from the Bi-Te film in Figure 4, where, for example, the 350 °C-2 h shows the best PF, and has the highest TEG power output (Figure 6) of 28 nW (for a TEG with 4 Bi-Te strips), which is much higher than the optimised result (<1 nW) for the Bi-Te fabricated by conventional magnetron sputtering.[60]

3. Conclusion

The HiTUS sputtering technique was used to fabricate functional thermoelectric thin films of bismuth telluride. Through a series of studies on the plasma power, the target power and the substrate bias, the thermoelectric performance (power factor) was improved from 3.2 to 6.5×10^{-4} W m^{-1} K^{-2}, to the authors' knowledge the highest for room-temperature sputtered bismuth telluride. The enhancement in power factor is ascribed to the adjustment of thermoelectric parameters, since the optimisation of HiTUS sputtering parameters enables us to alter the relationship between Seebeck coefficient and electrical resistivity in bismuth telluride films. This improvement is primarily attributed to changes in grain size, crystallite size, elemental composition, surface roughness, and other relevant factors. Compared with conventional sputtering, the sputtering power in HiTUS is separately controlled by the power in the plasma generator and the power applied on the target. Additionally, the magnetic field that guides the plasma also plays a significant role in the kinetic energy of the sputtered species and thus affects the material's property. From this good base position, post-deposition annealing further improved the film to be highly polycrystalline, resulting in a thermoelectric power factor of 23.5×10^{-4} W m^{-1} K^{-2} and a figure of merit ≈0.45 at room temperature.

This study demonstrated the HiTUS sputtered functional materials with excellent performance, as compared to the conventional magnetron sputtered materials, significantly boosting the application of the HiTUS technology in industrial manufacture, especially for roll-to-roll processing.

4. Experimental Section

Sample Fabrication: Thin films were sputtered at room temperature onto flexible polyimide sheets (*Dupont* Kapton 500 HN, 125 µm), in a HiTUS system (*Plasma Quest Ltd.*) using a 4-inch diameter sputtering target

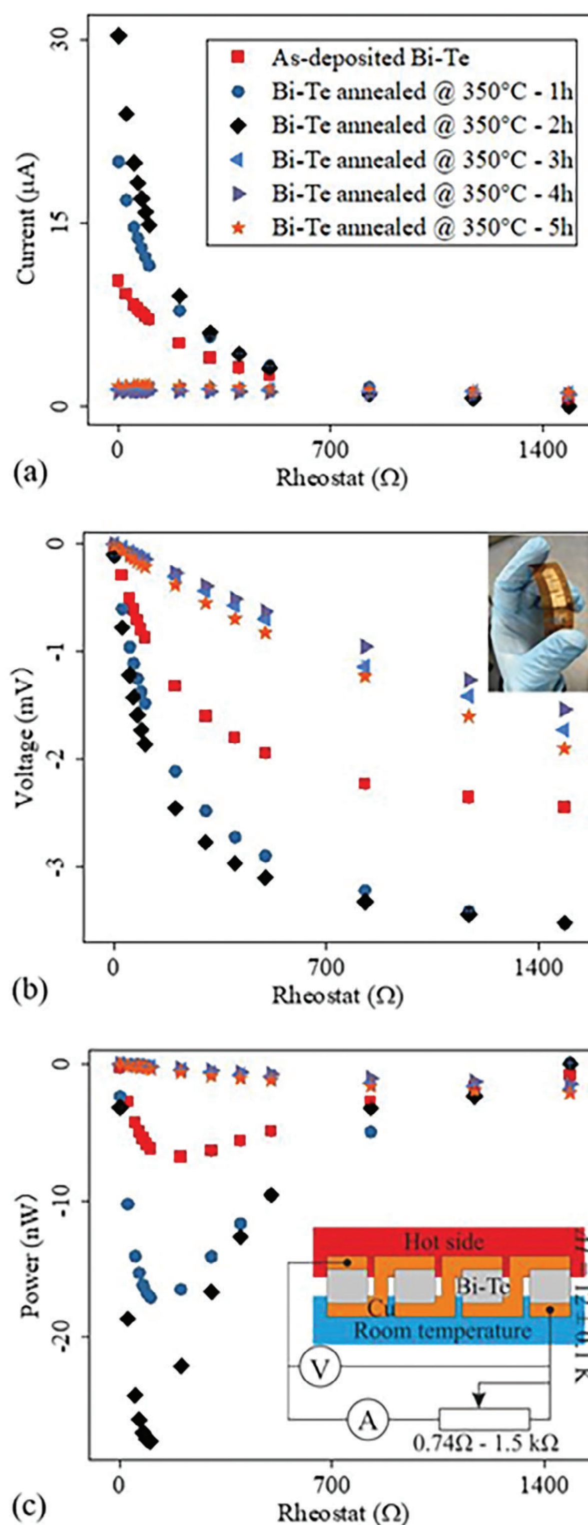

Figure 6. Thermoelectric measurement of current, voltage and power for the Bi-Te film annealed at 350 °C for 1–5 h. The picture inset (b) is a real image of the fabricated TEGs. The effective length of the TE strip = the total length of the strip (9 mm) – the length of the contact at two ends (3 mm + 3 mm). The "Z" shape patterns are the contact materials (Cu). ΔT represents the temperature difference which is set at 12 K during measurements.

© 2024 The Authors. Advanced Materials Technologies published by Wiley-VCH GmbH

2365709x, 0, Downloaded from https://onlinelibrary.wiley.com/doi/10.1002/admt.202301958 by Test, Wiley Online Library on [08/02/2024]. See the Terms and Conditions (https://onlinelibrary.wiley.com/terms-and-conditions) on Wiley Online Library for rules of use; OA articles are governed by the applicable Creative Commons License

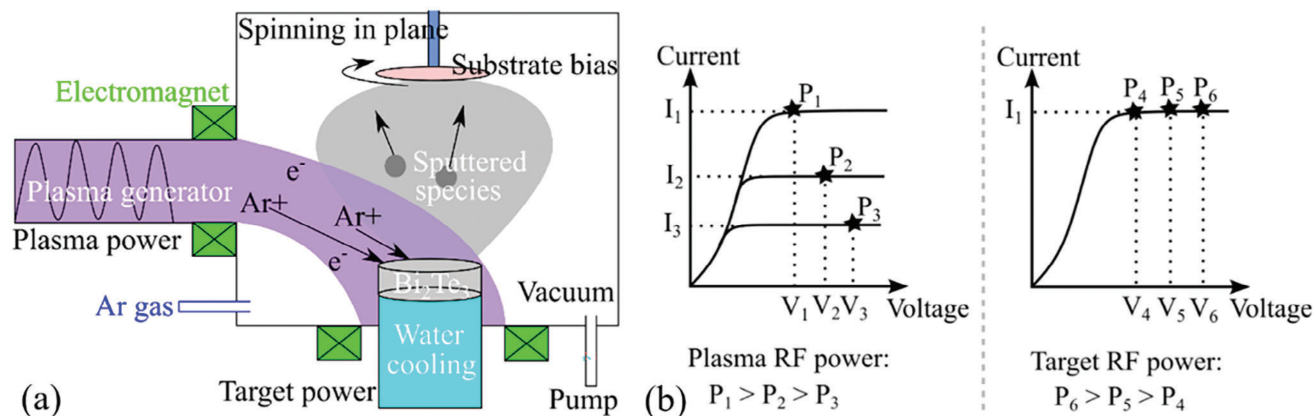

Figure 7. a) Schematic diagram of the HiTUS sputtering system; b) RF power applied to the plasma and the target (I and V denote the current and voltage, respectively, in the RF power systems. P = I × V). Plasma generator: as RF voltage across the plasma source and Ar gas is applied, a plasma is generated with induced current, with the voltage across the plasma dependent upon the plasma density (resistance). Target power: the electromagnets, under applied RF voltage, guide the plasma toward the target to induce sputtering. The target current is associated with the plasma density, i.e., the plasma source current. Substrate bias: the substrate bias is applied between the substrate holder and the ground, and the magnitude of this will modify the distribution of the plasma in the chamber. When a very high substrate bias is applied, the plasma may interact sufficiently with the substrate to modify the deposited film, e.g., by re-sputtering. In the substrate bias, RF power was supplied between the substrate holder and the ground (the chamber walls).

of Bi_2Te_3 (99.999% purity, *Mi-Net Technology Ltd.*) under a base pressure of 9×10^{-6} mbar. **Figure 7** shows a schematic representation of the system. 318 sccm Ar flow (6.4×10^{-3} mbar of working pressure) was fed into the plasma generator with various radio-frequency (RF) powers (0.6–1.2 kW), the target power (RF) was varied 0.4–1 kW, and the substrate holder was spinning at 20 rpm with a substrate bias of 0–125 W. The sputtering time was varied (5–14 mins) to control the film thickness at ≈500 nm. After optimisation of the sputtering parameters, the best film was selected for post-deposition annealing studies (as used in,[29] a vacuum pressure of 1×10^{-5} mbar, an annealing temperature of 350–450 °C, and an annealing time of 1–5 h). We did not observe any shape changes in the polyimide or encounter delamination issues with bismuth telluride, as for previous works.[29,61,62]

The optimised TE materials were then utilised to fabricate a single type[60,63] thermoelectric generator (TEGs) by sputtering through flexible polymer masks. The effective length and width of TE strips in TEGs were fixed at ≈3 and ≈6 mm, respectively. The contact materials to connect TE strips were ≈310-nm thick Cu film (sheet resistance ≈1 Ω sq^{-1}) fabricated by thermal evaporation through flexible polymer masks using Oxford R2R web coater (*Aerre Machines*) with samples taped to a rotating drum (circumference 1.8 m) that passes repeatedly under the evaporation source, under a base pressure of 1.3×10^{-4} mbar, a deposition time of 2 min, a current of 605 A through a ceramic boat (*Sintec Ceramics*) and a drum in-line speed of 25 m min^{-1}.

Sample Characterisation: The film thickness was measured using *Veeco DekTak* 6 M stylus profilometer by a step-masked region on a polyimide sheet using polyimide tapes before deposition. At least eight locations were measured for an average in each case.

XRD data were collected using *Rigaku Miniflex* diffractometer under Cu k_α radiation, $\lambda = 0.154$ nm, step size = 0.007°, 2Theta = 10°–80°, 40 kV, 40 mA. The *Highscore plus* software was used to analyse data for the crystallite size using the Williamson-Hall method.[64]

Held by the single-tilt holder (±25°), a high-vacuum *JEOL* 3000F analytical HRTEM was used to characterise the film morphology and crystallinity under 200 keV. ≈45-nm thick films were prepared onto a lacey carbon-supported copper grid (300 mesh, *Agar Scientific*) and air dried for 2 hours prior to observation. HRTEM data were then processed using the Gatan Digital Micrograph software.

The film surface morphology was characterised by a field-emission SEM (*Zeiss Merlin*) and AFM (*Agilent* 5400). AFM was conducted in tapping mode using the tip (NCHV–A) from *Bruker Ltd.*, analysed using software *WSxM* 5.0 Develop 9.0 (for the surface roughness) and *MIPAR* (for the grain size). SEM images were captured under 100 kX of the magnification, 3 kV voltage, 100 pA current probe, and 3 mm working distance. EDX integrated with the SEM was used to characterise the elemental composition of Bi-Te films over 15 locations, under 8 mm working distance, 5 kV voltage and 2.5 kX magnification.

A Seebeck system (*MMR Technologies Inc.*) was used to measure the in-plane Seebeck coefficient of Bi-Te films, under a temperature difference of 0.1–0.45 K in a nitrogen atmosphere. Three identical samples were measured for an average in each case.

The sheet resistance (R_s) of the film was measured over eight locations, using a four-point probe system by applying a current of 0.1–1 mA in the outer two probes and measuring voltage in the two inner probes using a *Keithley* source meter. Then the electrical resistivity was calculated by a product of the film thickness and R_s.

The carrier mobility (μ) and concentration (n) were measured at room temperature using an in-house custom Hall measurement system (0.165 T magnet) with a van der Pauw configuration using *Keysight* B2901A.

UV-Visible-NIR spectrometer (*Cary Varian* 5000) was used to obtain the absorbance spectra (200–3300 nm), for the analysis of the Tauc plot for bandgap. The Figure S12 (Supporting Information) shows example Tauc plots for the analysis of indirect and direct E_g. Co-existence of the indirect and direct E_g of Bi_2Te_3 has already been studied, e.g. the temperature-dependence[65,66] and location-dependence.[67,68]

To obtain the total κ, the κ_e and the κ_L can be calculated separately by the Wiedemann–Franz law and the Debye–Callaway model, respectively. See Appendix for details.

The κ was also obtained by experimental measurements through 1) the pseudo steady-state 3-ω method using a *Linseis* Thin Film Analyser, where the thin film was deposited on the membrane of a pre-patterned measurement chip; 2) the thermal diffusivity of Bi-Te film grown on a polyimide sheet was measured using the laser-induced transient grating spectroscopy method,[69] then the κ was calculated by a product of thermal diffusivity (as measured), specific heat capacity and mass density of Bi-Te (165 J kg^{-1} K^{-1} and 7.60 g cm^{-3}, respectively, referenced from[53]).

An in-house custom Seebeck setup was utilised to assess the performance of TEGs. Two Peltier modules (*European Thermodynamics Ltd.*) applied ΔT to the TEGs, and the voltage output (U) was measured across a simple Ohm's circuit (with a load resistance R_L equal to the internal resistance of TEGs R_{TEG}[70] to maximize the power output $P = U^2/R_L$).

© 2024 The Authors. Advanced Materials Technologies published by Wiley-VCH GmbH

2365709x, 0, Downloaded from https://onlinelibrary.wiley.com/doi/10.1002/admt.202301958 by Test, Wiley Online Library on [08/02/2024]. See the Terms and Conditions (https://onlinelibrary.wiley.com/terms-and-conditions) on Wiley Online Library for rules of use; OA articles are governed by the applicable Creative Commons License

Supporting Information

Supporting Information is available from the Wiley Online Library or from the author.

Acknowledgements

The authors would like to acknowledge the funding from the Engineering and Physical Sciences Research Council [EPSRC grant number EP/M015173/1] and the EPSRC Impact Acceleration Account Award [EP/R511742/1]. O.F. is funded by the Royal Society University Research Fellowship (URF/R/201013). R.S.B. is supported by the Royal Academy of Engineering under the Research Fellowship scheme (RF\201819\18\38). Transient grating spectroscopy measurements were supported by ERC starting grant "AtoFun" 714697. The authors are also grateful for the equipment access from Oxford Materials Characterization Services and Oxford Materials and David Cockayne Centre for Electron Microscopy.

Conflict of Interest

The authors declare no conflict of interest.

Data Availability Statement

The data that support the findings of this study are available from the corresponding author upon reasonable request.

Keywords

bismuth telluride, flexible electronics, remote-plasma sputtering, thermoelectric thin film

Received: November 15, 2023
Revised: January 16, 2024
Published online:

[1] Y. Yang, Z. Lin, T. Hou, F. Zhang, Z. L. Wang, *Nano Res.* **2012**, *5*, 888.
[2] R. Feng, F. Tang, N. Zhang, X. Wang, *ACS Appl. Mater. Interfaces* **2019**, *11*, 38616.
[3] Y. Wang, W. Zhu, Y. Deng, B. Fu, P. Zhu, Y. Yu, J. Li, J. Guo, *Nano Energy* **2020**, *73*, 104773.
[4] H. Cheng, Y. Du, B. Wang, Z. Mao, H. Xu, L. Zhang, Y. Zhong, W. Jiang, L. Wang, X. Sui, *Chem. Eng. J.* **2018**, *338*, 1.
[5] J. Yuan, R. Zhu, *Appl. Energy* **2020**, *271*, 115250.
[6] J. Yuan, R. Zhu, G. Li, *Adv. Mater. Technol.* **2020**, *5*, 2000419.
[7] A. Bansal, R. Joshi, *J. Arrhyth.* **2018**, *34*, 129.
[8] C. S. Kim, H. M. Yang, J. Lee, G. S. Lee, H. Choi, Y. J. Kim, S. H. Lim, S. H. Cho, B. J. Cho, *ACS Energy Lett.* **2018**, *3*, 501.
[9] J. Kim, S. Khan, P. Wu, S. Park, H. Park, C. Yu, W. Kim, *Nano Energy* **2021**, *79*, 105419.
[10] Y. J. Kim, H. M. Gu, C. S. Kim, H. Choi, G. Lee, S. Kim, K. K. Yi, S. G. Lee, B. J. Cho, *Energy* **2018**, *162*, 526.
[11] V. Leonov, T. Torfs, P. Fiorini, C. Van Hoof, *JSEN* **2007**, *7*, 650.
[12] D. Brunelli, R. Passerone, L. Rizzon, M. Rossi, D. Sartori, *Sensors* **2016**, *16*, 57.
[13] L. Huang, J. Chen, Z. Yu, D. Tang, *Analytical chemistry (Washington)* **2020**, *92*, 2809.
[14] F. Zhang, Y. Zang, D. Huang, C. Di, D. Zhu, *Nat. Commun.* **2015**, *6*, 8356.
[15] P. Zhu, Y. Wang, Y. Wang, H. Mao, Q. Zhang, Y. Deng, *Adv. Energy Mater.* **2020**, *10*, 2001945.
[16] M. Li, J. Chen, W. Zhong, M. Luo, W. Wang, X. Qing, Y. Lu, Q. Liu, K. Liu, Y. Wang, D. Wang, *ACS Sens.* **2020**, *5*, 2545.
[17] S. Park, S. Yoon, C. Lee, Y. Kim, S. Song, *Analyst* **2009**, *134*, 236.
[18] M. Nishibori, W. Shin, N. Izu, T. Itoh, I. Matsubara, *Sens. Actuators, B* **2009**, *137*, 524.
[19] D. XU, Y. WANG, B. XIONG, T. LI, *Front. Mech. Eng.* **2017**, *12*, 557.
[20] X. Zhang, Y. Hou, Y. Yang, Z. Wang, X. Liang, Q. He, Y. Xu, X. Sun, H. Ma, J. Liang, Y. Liu, W. Wu, H. Yu, H. Guo, R. Xiong, *Adv. Mater.* **2022**, *35*, 2207723.
[21] Z. Fan, Y. Zhang, L. Pan, J. Ouyang, Q. Zhang, *Renew. Sust. Energ. Rev.* **2021**, *137*, 110448.
[22] K. Biswas, J. He, I. D. Blum, C. Wu, T. P. Hogan, D. N. Seidman, V. P. Dravid, M. G. Kanatzidis, *Nature* **2012**, *489*, 414.
[23] D. K. Bhat, U. S. Shenoy, *Mater. Today Phys.* **2019**, *11*, 100158.
[24] D. Liu, D. Wang, T. Hong, Z. Wang, Y. Wang, Y. Qin, L. Su, T. Yang, X. Gao, Z. Ge, B. Qin, L. Zhao, *Science* **2023**, *380*, 841.
[25] U. S. Shenoy, D. K. Bhat, *J. Mater. Chem.* **2020**, *8*, 2036.
[26] O. Oluwatosin Abegunde, E. Titilayo Akinlabi, O. Philip Oladijo, S. Akinlabi, A. Uchenna Ude, *AIMS Mater. Sci.* **2019**, *6*, 174.
[27] X. Tao, K. Wan, J. Deru, E. Bilotti, H. E. Assender, *Surf. Coat. Technol.* **2020**, *385*, 125393.
[28] X. Tao, K. Wan, B. W. Stuart, E. Bilotti, H. E. Assender, *Thin Solid Films* **2020**, *712*, 138311.
[29] X. Tao, B. W. Stuart, K. Wan, J. W. Murray, E. Bilotti, H. E. Assender, *ACS Appl. Mater. Interfaces* **2021**, *13*, 10149.
[30] X. Tao, K. Zhang, B. W. Stuart, H. E. Assender, *Surf. Coat. Technol.* **2022**, *434*, 128167.
[31] Z. Chen, G. Han, L. Yang, L. Cheng, J. Zou, *Prog. Nat. Sci.: Mater. Int.* **2012**, *22*, 535.
[32] B. W. Stuart, X. Tao, D. Gregory, H. E. Assender, *Appl. Surf. Sci.* **2019**, *505*, 144294.
[33] X. Tao, B. W. Stuart, H. E. Assender, *Surf. Coat. Technol.*, https://doi.org/10.1016/j.surfcoat.2022.128826.
[34] B. W. Stuart, K. Morgan, X. Tao, I. Zeimpekis, Z. Feng, D. Gregory, H. E. Assender, *Coatings* **2021**, *11*, 1470.
[35] J. P. Fleurial, L. Gailliard, R. Triboulet, H. Scherrer, S. Scherrer, *J. Phys. Chem. Solids* **1988**, *49*, 1237.
[36] I. T. Witting, T. C. Chasapis, F. Ricci, M. Peters, N. A. Heinz, G. Hautier, G. J. Snyder, *Adv. Electron. Mater.* **2019**, *5*, 1800904.
[37] H. L. Brown, S. A. Thornley, S. J. Wakeham, M. J. Thwaites, R. J. Curry, M. A. Baker, *J. Phys. D* **2015**, *48*, 335303.
[38] Y. Li, Q. Xin, L. Du, Y. Qu, H. Li, X. Kong, Q. Wang, A. Song, *Sci. Rep.* **2016**, *6*, 36183.
[39] M. Yamada, J. Yoo, J. Jara-Almonte, H. Ji, R. M. Kulsrud, C. E. Myers, *Nat. Commun.* **2014**, *5*, 4774.
[40] J. Gong, X. Zhang, Z. Pei, C. Sun, L. Wen, *J. Mater. Sci. Technol.* **2011**, *27*, 393.
[41] H. Ohsaki, Y. Shibayama, A. Nakajim, A. Kinbara, T. Watanabe, *Thin Solid Films* **2006**, *502*, 63.
[42] J. Park, D. C. Kim, Y. Kim, *Thin Solid Films* **2017**, *622*, 111.
[43] C. Wood, *Rep. Prog. Phys.* **1988**, *51*, 459.
[44] I. Petsagkourakis, E. Pavlopoulou, E. Cloutet, Y. F. Chen, X. Liu, M. Fahlman, M. Berggren, X. Crispin, S. Dilhaire, G. Fleury, G. Hadziioannou, *Org. Electron.* **2018**, *52*, 335.
[45] G. J. Snyder, E. S. Toberer, *Nat. Mater.* **2008**, *7*, 105.
[46] E. M. Levin, *Phys. Rev. B.* **2016**, *93*, 2452021.
[47] H. Marom, M. Eizenberg, *J. Appl. Phys.* **2006**, *99*, 123705.
[48] S. Munir, S. M. Shah, H. Hussain, R. A. khan, *Mater. Des.* **2016**, *92*, 64.
[49] V. Linseis, F. Völklein, H. Reith, K. Nielsch, P. Woias, *Rev. Sci. Instrum.* **2018**, *89*, 015110.

© 2024 The Authors. Advanced Materials Technologies published by Wiley-VCH GmbH

2365709x, 0, Downloaded from https://onlinelibrary.wiley.com/doi/10.1002/admt.202301958 by Test, Wiley Online Library on [08/02/2024]. See the Terms and Conditions (https://onlinelibrary.wiley.com/terms-and-conditions) on Wiley Online Library for rules of use; OA articles are governed by the applicable Creative Commons License

[50] T. Liu, X. Zhao, J. Li, Z. Liu, F. Liscio, S. Milita, B. C. Schroeder, O. Fenwick, *Nat. Commun.* **2019**, *10*, 5750.
[51] C. A. Dennett, M. P. Short, *Appl. Phys. Lett.* **2017**, 110.
[52] A. Reza, C. A. Dennett, M. P. Short, J. Waite, Y. Zayachuk, C. M. Magazzeni, S. Hills, F. Hofmann, *Rev. Sci. Instrum.* **2020**, *91*, 054902.
[53] T. Arisaka, M. Otsuka, Y. Hasegawa, *Rev. Sci. Instrum.* **2019**, *90*, 046104.
[54] M. Naumochkin, G. Park, K. Nielsch, H. Reith, *Physica Status Solidi. Pss-rrl. Rapid Research letters* **2022**, *16*, https://doi.org/10.1002/pssr.202100533.
[55] A. Soni, Z. Yanyuan, Y. Ligen, M. K. K. Aik, M. S. Dresselhaus, Q. Xiong, *Nano Lett.* **2012**, *12*, 1203.
[56] Y. Zhang, H. Wang, S. Kräemer, Y. Shi, F. Zhang, M. Snedaker, K. Ding, M. Moskovits, G. J. Snyder, G. D. Stucky, *ACS Nano* **2011**, *5*, 3158.
[57] S. Sumithra, N. J. Takas, D. K. Misra, W. M. Nolting, P. F. P. Poudeu, K. L. Stokes, *Adv. Energy Mater.* **2011**, *1*, 1141.
[58] M. Han, J. Hwang, S. Kim, *J. Mater. Sci.: Mater. Electron.* **2019**, *30*, 1282.
[59] J. S. Son, M. K. Choi, M. Han, K. Park, J. Kim, S. J. Lim, M. Oh, Y. Kuk, C. Park, S. Kim, T. Hyeon, *Nano Lett.* **2012**, *12*, 640.
[60] X. Tao, K. Zhang, D. Gregory, J. Liu, H. E. Assender, *Energy Technol.* **2021**, *9*, 2001008.
[61] K. Singkaselit, A. Sakulkalavek, R. Sakdanuphab, *ANSN* **2017**, *8*, 350021.
[62] S. Kianwimol, R. Sakdanuphab, N. Chanlek, A. Harnwunggmoung, A. Sakulkalavek, *Surf. Coat. Technol.* **2020**, *393*, 125808.
[63] X. Tao, B. Hao, H. E. Assender, *Adv. Electron. Mater.* **2021**, *7*, 2100201.
[64] G. K. Williamson, W. H. Hall, *Acta Metall.* **1953**, *1*, 22.
[65] M. Hada, K. Norimatsu, S. Tanaka, S. Keskin, T. Tsuruta, K. Igarashi, T. Ishikawa, Y. Kayanuma, R. J. D. Miller, K. Onda, T. Sasagawa, S. Koshihara, K. G. Nakamura, *J. Chem. Phys.* **2016**, *145*, 024504.
[66] G. A. Thomas, D. H. Rapkine, R. B. Van Dover, L. F. Mattheiss, W. A. Sunder, L. F. Schneemeyer, J. V. Waszczak, *Phys. Rev. B Condens.* **1992**, *46*, 1553.
[67] M. Michiardi, I. Aguilera, M. Bianchi, V. E. de Carvalho, L. O. Ladeira, N. G. Teixeira, E. A. Soares, C. Friedrich, S. Blügel, P. Hofmann, **2014**, *90*, 075105.
[68] P. Larson, S. D. Mahanti, M. G. Kanatzidis, *Phys. Rev. B Condens.* **2000**, *61*, 8162.
[69] A. Reza, H. Yu, K. Mizohata, F. Hofmann, *Acta Mater.* **2020**, *193*, 270.
[70] D. Enescu, *Green Energy Advances*, IntechOpen, London, UK **2019**.

© 2024 The Authors. Advanced Materials Technologies published by Wiley-VCH GmbH

2365709x, 0, Downloaded from https://onlinelibrary.wiley.com/doi/10.1002/admt.202301958 by Test, Wiley Online Library on [08/02/2024]. See the Terms and Conditions (https://onlinelibrary.wiley.com/terms-and-conditions) on Wiley Online Library for rules of use; OA articles are governed by the applicable Creative Commons License